Journal of Alloys and Compounds 509 (2011) 2909–2913

Contents lists available at ScienceDirect

Journal of Alloys and Compounds

journal homepage: www.elsevier.com/locate/jallcom

Structural, optical and transport properties of Al^{3+} doped $BiFeO_3$ nanopowder synthesized by solution combustion method

Ameer Azam [a,b,*], Ali Jawad [b], Arham S. Ahmed [b], M. Chaman [b], A.H. Naqvi [b]

[a] Centre of Nanotechnology, King Abdulaziz University, Jeddah, Saudi Arabia
[b] Department of Applied Physics, Z.H. College of Engineering & Technology, Aligarh Muslim University, Aligarh 202002, U.P., India

ARTICLE INFO

Article history:
Received 24 August 2010
Received in revised form
19 November 2010
Accepted 23 November 2010
Available online 1 December 2010

Keywords:
d.c. resistivity
Band gap
Auto combustion
Bismuth ferrite
XRD
FTIR

ABSTRACT

Aluminum doped Bismuth ferrite (BFO) nanopowders (grain size 13–20 nm) having composition $Bi_{1-x}Al_{2x}Fe_{1-x}O_3$ (x = 0.00, 0.025, 0.05, 0.10, 0.15, 0.20, 0.25 and 0.30) were successfully synthesized by solution combustion method using citric acid as fuel at a temperature as low as 200 °C. As-prepared samples were examined by powder XRD for phase identification and crystallite size determination. The d.c. resistivity as a function of temperature was measured by standard two probe setup which exhibits clear metal to insulator transition for all samples. FTIR analysis was carried out to identify the chemical bonds present in the system. The optical band gap was calculated from the UV–vis absorbance spectra using classical Tauc relation which was found to vary from 2.78 eV to 2.93 eV for different Al^{3+} concentrations. The activation energies calculated from the slopes of $\ln(\rho)$ versus $10^3/T$ plots are in the range 0.54–0.73 eV.

1. Introduction

$BiFeO_3$ (BFO) is a perovskite material which potentially exhibits simultaneous coexistence of ferroelectric and antiferromagnetic ordering having Curie temperature (T_c) 1083 K and Neil temperature (T_n) 657 K [1]. The recent investigations have suggested that this material is very promising material for its possible applications especially in the fields of radio transmission, microwave and satellite communication, digital recording, and permanent magnet applications. Bismuth and its compounds may hold the key for future electronics due to their highly frustrated structures. BFO is not new but in the earlier years of its birth it failed to make any remarkable impact on the then electronic industries due to problem of leakage current that was rooted in nonstoichiometry. The main reason is that the BFO nanopowders synthesized by even established methods are generally plagued by impure phases. In its bulk form, measurements of ferroelectric and transport properties in BFO and its derivatives have been limited by the problem of leakage, mainly due to low resistivity, lattice defects and nonstoichiometry.

The properties of BFO can be tailored significantly by chemical substitution at both Bi and Fe sites. There are many reports on the site substituted BFO recipes. Li et al. investigated the Sr doping on Bi site, resulting the samples being oxygen substoichiometric [2]. Further, they concluded that with the increase of Sr concentration, $SrFeO_3$ phase evolves which leads to diminished magnetization. Similar results were obtained by Khomchenko et al. with Ca and Ba doped BFO [3]. Lee et al. prepared La doped BFO thin films with increased dielectric constant and remnant polarization which they attributed to the increased crystallanity and lattice volume with La doping [4]. Further, La doped BFO ceramics exhibited improved magnetization due to phase transition [5]. Another report confirms the enhancement in multiferroic properties of La doped BFO samples which they attributed to the enhanced magnetoelectric interaction [6]. Al^{3+} doping at Bi site has been investigated for photocatalytic applications by Madhu et al. [7]. To the best of our knowledge no report is available on the transport properties of Al^{3+} doped $BiFeO_3$ nanopowder. This paper presents the investigation of the optical properties and transport behavior in terms of d.c. resistivity of the BFO samples doped by Al^{3+} at both Bi and Fe sites.

2. Experimental

In a typical synthesis procedure, stoichiometric amounts of $Bi(NO_3)_3{\cdot}5H_2O$ (99.00%, S.D. Fine Chemicals), $Fe(NO_3)_3{\cdot}9H_2O$ (98.00%, S.D. Fine Chemicals) and $Al(NO_3)_3{\cdot}9H_2O$ (95%, Merck Chemicals) were dissolved in minimum amount of double distilled water. All chemicals were of reagent grade and used without further purification. As $Bi(NO_3)_3{\cdot}5H_2O$ undergoes decomposition into bismuth oxychloride

* Corresponding author at: Department of Applied Physics, Z.H. College of Engineering & Technology, Aligarh Muslim University, Aligarh 202002, U.P., India. Tel.: +966 567715481.
E-mail addresses: azam222@rediffmail.com, ameerazam2009@gmail.com (A. Azam).

0925-8388/$ – see front matter © 2010 Elsevier B.V. All rights reserved.
doi:10.1016/j.jallcom.2010.11.153

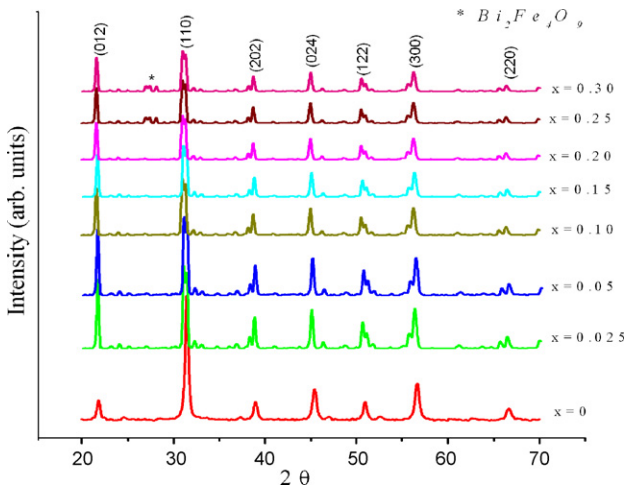

Fig. 1. XRD spectra of Al^{3+} doped $BiFeO_3$ nanopowder.

in water, it was first taken in 15 ml water and kept on stirring. During stirring HNO_3 was added drop by drop until a clear and transparent solution is obtained which confirms the complete dissolution of $Bi(NO_3)_3{\cdot}5H_2O$. At this point $Fe(NO_3)_3{\cdot}9H_2O$ and Al $(NO_3)_3{\cdot}9H_2O$ were added to the solution and kept for further stirring up to complete dissolution. The stoichiometric amount of citric acid ($C_6H_8O_7$) necessary for the complete combustion of the nitrates was calculated according to propellant chemistry expression:

$$\Psi = \frac{\text{total oxidising valence of oxidising agents (nitrates)}}{\text{total oxidising valence of reducing agents (fuel)}}$$

For citric acid, the total reducing valence is $F = 18$ and for each trivalent nitrate the oxidizing valence is $O = 15$. So, for complete combustion $O/F = 15/18 = 0.833$. Thus for each nitrate, the nitrate to fuel ratio becomes 1:0.833. This concludes that for the complete combustion of the system, {[Bi $(NO_3)_3]_{1-x} + xAl(NO_3)_3$}:{[$Fe(NO_3)_3]_{1-x} + xAl(NO_3)_3$}:citric acid = 1:1:1.666, accordingly the calculated stoichiometric amount of citric acid will be 3.2007 g (taking 0.01 M). Assuming the complete combustion the process may be:

$$6Fe(NO_3)_3 + 6Bi(NO_3)_3 + 10C_6H_8O_7 = 6BiFeO_3 + 18N_2 + 60CO_2 + 40H_2O$$

$$\{[Bi(NO_3)_3]_{1-x} + xAl(NO_3)_3\} + \{[Fe(NO_3)_3]_{1-x} + xAl(NO_3)_3\} + 10C_6H_8O_7$$
$$= 6Bi_{1-x}Al_{2x}Fe_{1-x}O_3 + 18N_2 + 60CO_2 + 40H_2O$$

The solution was kept on a hot plate maintained initially at 50 °C for 30 min while stirring continuously with a nonmagnetic stirrer. Soon the water evaporates and a very viscous transparent honey like gel is formed. The as-prepared gel was immediately put inside a furnace preheated at 200 °C. The ignition starts which uniformly propagates through the gel. Huge amount of brown fumes evolve towards the end of the reaction. Whole process completes within 5 min resulting a fluffy and foamy green mass. This porous mass was ground for 30 min and sintered at 500 °C for 3 h at a heating rate of 5 °C min^{-1}. One gram quantity of each sample was mixed with 2% PVA and compressed in the form of circular pellets of 13 mm diameter. All pellets were again heated at 400 °C to evaporate the binding agent. The powders were examined for crystallanity, phase identification and crystallite size determination by X-ray diffraction (Rigaku, Japan) using Cu-K_α radiations ($\lambda = 0.15406$ nm) in 2θ range from 20° to 70° with scan rate of 2°/min and a step size of 0.02°. UV–vis absorbance was taken using Perkin Elmer spectrophotometer. FT-IR spectroscopy was performed on Perkin Elmer spectrometer using KBr as medium. d.c. resistivity was measured using Keithley's standard two probe set up.

3. Results and discussion

3.1. Structural properties

Fig. 1 shows X-ray diffraction patterns of synthesized powders sintered in air at 500 °C for 3 h. The peaks were indexed using Powder-X software and they are well matched with the rhombohedrally distorted perovskite structure. The powder patterns are in good agreement with the standard ICDD card no. 86-1518. XRD results revealed the formation of single phase material up to $x = 0.20$ beyond which a minute impurity phase was observed in the form of $Bi_2Fe_4O_9$ at $x = 0.25$ and 0.30. The crystallite sizes for different samples were calculated using Scherer's equation $D = 0.9\lambda/\beta\cos\theta$, where D is the average crystallite diameter, $\lambda = 1.5406$ Å (characteristic Cu-K_α wavelength of X-rays) and β is the width of the diffraction peak at half of the maximum height (FWHM) for diffraction angle 2θ. The crystallite size calculated for different samples varies from 13.0 nm to 19.6 nm. It is evident from XRD spectra that peak intensity decreases while FWHM increases with the increase in dopant concentration, which shows the reduction in crystallite size. The lattice parameters of the unit cell were calculated using the equation:

$$\sin^2\theta = \frac{\lambda^2}{3\alpha^2}(h^2 + hk + k^2) + \frac{\lambda^2 l^2}{4c^2}$$

where θ is Bragg's angle [8]. The strong peaks (0 1 2) and (1 1 0) were employed for such calculations. The lattice parameters a and c, crystallite size, volume of the unit cell V, and the ratio c/a are listed in Table 1, which are in good agreement with values reported in literature [3,9–11]. Further, it is evident from Table 1 that crystallite size, lattice parameter and cell volume decrease with the increase in Al^{3+} concentration which may be attributed to the shortened ionic radius of Al^{3+} (0.053 nm) compared to Fe^{3+} (0.064 nm) and Bi^{3+} (0.074 nm).

Table 1
Variation of lattice parameters a and c, c/a ratio, cell volume of the unit cell and grain size with composition.

x	a (Å)	c (Å)	c/a	Cell volume	Grain size (nm)
0.000	5.595	13.862	2.477	373.54	19.64
0.025	5.581	13.860	2.483	372.62	17.53
0.050	5.547	13.859	2.498	371.88	16.72
0.100	5.529	13.851	2.505	370.73	15.57
0.150	5.518	13.846	2.509	370.02	15.01
0.200	5.512	13.843	2.511	369.51	14.43
0.250	5.507	13.838	2.512	369.02	13.65
0.300	5.502	13.0830	2.513	368.57	13.02

Fig. 2 exhibit the FTIR spectra of all samples recorded in wavenumber range 400–1000 cm^{-1}. The spectra in this range are indicative of the perovskite type vibrations. The two strong absorption bands around 445 cm^{-1} and 552 cm^{-1} for all samples are attributed to O–Fe–O bending vibrations and Fe–O stretching of FeO_6 groups in perovskite structure [12]. Other small peaks in the range 400–600 cm^{-1} give a clear signature of C–C and M–C–O bonding, thereby indicating the presence of very small amount of carbonaceous materials which are left after the combustion of fuel. The band at 650 cm^{-1} corresponds to the bending modes of vibra-

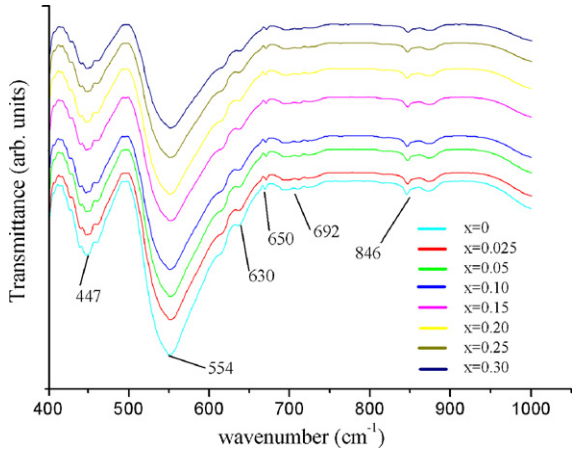

Fig. 2. FTIR spectra of all the samples with different concentrations of Al^{3+} ions.

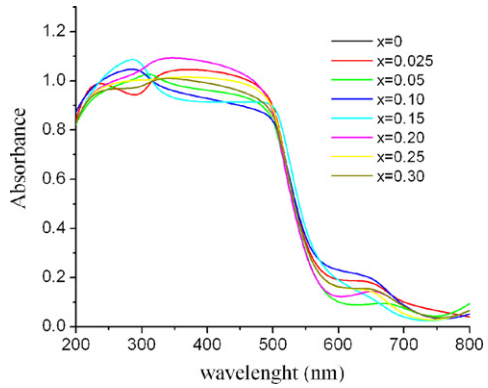

Fig. 3. UV–vis absorbance of all the samples depicting strong UV absorption over a wide range.

tions of Al_2O_3 and at 630 cm^{-1} corresponds to the bending modes of vibrations of oxides of bismuth. It is evident from the spectra that there is a minor shift in the IR active modes of different samples which is mainly due to the presence of nano-sized grains. This can be attributed to the fact that in the case of nano size grains the arrangement of atoms at the grain boundaries are different from that of the bulk crystals. This leads to disorders in both the coordination number and bond length and this degradation in crystal symmetry is responsible for the shifting in IR active modes [13]. The IR results are in good agreement with those reported earlier in literature [14–16].

3.2. Optical properties

It is well known that the properties of optical absorption (UV–vis) by semiconductors are relevant to the electronic structure features and hence are the key factors in determining their band gaps [17]. The UV–vis absorption spectra of all samples are shown in Fig. 3, which is in good agreement to the typical BFO UV–vis absorbance spectra reported elsewhere [18,19]. The optical energy band gap for different samples was calculated by classical Tauc relation [20] as given below:

$$\alpha h\nu = A(h\nu - E_g)^n$$

where A is a constant, $h\nu$ is the photon energy, E_g is the energy band gap, α is absorption coefficient given by $\alpha = 2.303(A_b/t)$, where, A_b is absorbance and t is the thickness of cuvette which is 1 cm in the present case. The value of $n = 1/2$, 3/2, 2, or 3 depending on the nature of the electronic transition responsible for absorption. The value of $n = 1/2$ allows for direct transition, thereby giving direct band gap. The absorption spectrum shows that BFO and its Al^{3+} derivatives can absorb considerable amount of visible light making them potentially usable for photochemical reactions. The plots of $(\alpha h\nu)^2$ versus $h\nu$ for all samples are shown in Fig. 4. Extrapolation of linear region of these plots to $(\alpha h\nu)^2 = 0$ gives corresponding direct energy band gap. It is evident from graphs that the direct band gap for all samples increases with the increase of Al^{3+} concentration and varies from 2.78 eV to 2.93 eV. These band gaps are relatively higher as compared to their bulk counterparts, being1.82 eV for BFO microspheres (20 μm), 2.12 eV for BFO microcubes (5 μm) and 2.27 eV for BFO submicrocubes (500 nm) [17], indicating that the band gap increases as the particle size approaches to nano regime. In some of the ternary semiconductors (like $InAs_xP_{1-x}$) it has been observed that band gap decreases with the increase in lattice parameters [21]. Therefore, increase of band gap in the present study with the Al^{3+} concentration can also be explained on the basis of the decrease in the lattice parameters which is due to smaller size of Al^{3+} (ionic radii = 0.053 nm) as compared to Fe (ionic radii = 0.064 nm) and Bi (ionic radii = 0.074 nm).

3.3. Electrical transport properties (d.c. resistivity)

Fig. 5 presents the plot of d.c. resistivity as a function of temperature for various samples. The general trend for all samples is almost the same. The resistivity increases in the temperature range 275–325 K, reaching maximum at around 325 K, beyond which it gradually decreases at higher temperatures. All samples initially manifest metallic behavior at low temperature and at higher temperatures, semiconducting behavior is highlighted. Thus, there is a clear metal to insulator transition which is a behavior typical to manganites and other perovskites. The metal to insulator transition temperature (T_{MI}) in the present case is equal to 325 K. Furthermore, the resistivity increases with the increase in Al^{3+} concentrations for whole range of temperature. This may be due to the interactions among various types of carrier species (electrons, holes, phonons) in the sample resulting in a strong scattering which in turn gives rise to elevated resistivity. The whole plot can be divided into two distinct regions, metallic region (below T_{MI}) and insulating region (above T_{MI}). In the metallic region, the resistivity can be explained on the basis of the model $\rho(T) = \rho_0 + \beta T^2 + \gamma T^r$,

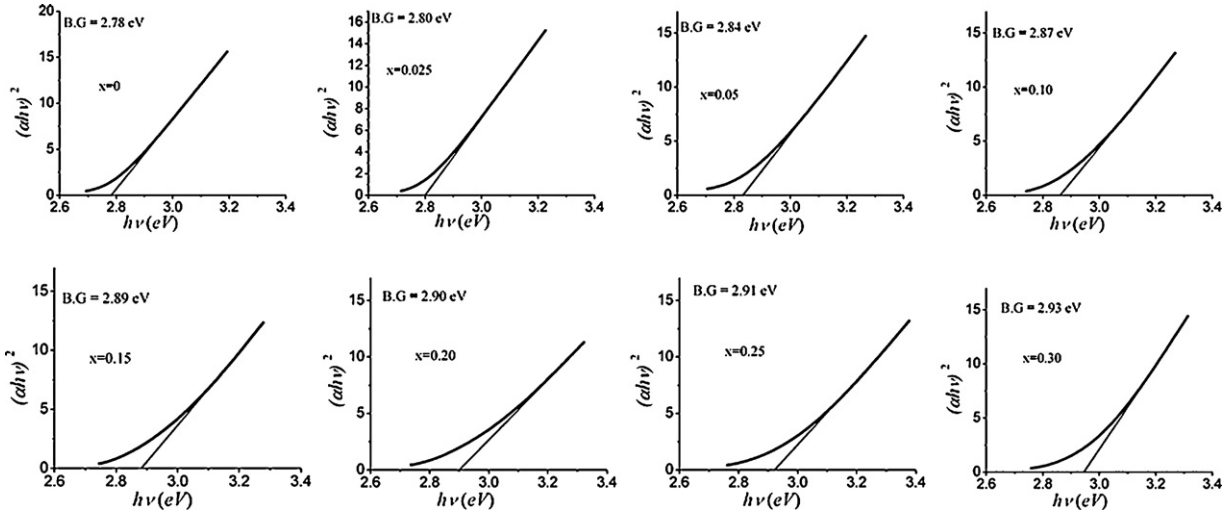

Fig. 4. Plots of $(\alpha h\nu)^2$ versus $h\nu$ for all the eight samples.

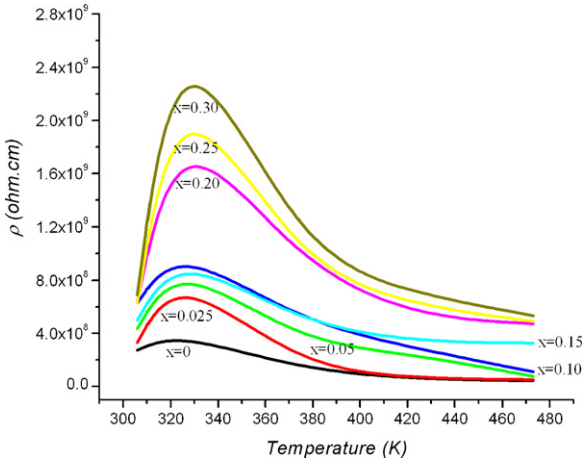

Fig. 5. d.c. resistivities as a function of temperature for different compositions.

where ρ_0 is residual resistivity at $T=0$, β the electron–electron (e–e) scattering coefficient and γ the electron–phonon (e–p) or electron–magnon (e–m) scattering coefficient. The value of $r \approx 5$ and 4.5 for e–p and e–m scattering respectively. In the insulating region, temperature causes the excitation of electrons to the conduction band, hence the resistivity can be considered as a thermally activated process. There are various models which explain the resistivity of insulators in the form of thermally activated behavior. Jonker and van Santen [22] suggested the model:

$$\rho(T) = A \exp\left(\frac{E_0}{k_B T}\right) \quad (1)$$

where E_0, k_B, A are activation energy, Boltzmann's constant and dependency of charge carriers on mobility respectively. A strong coupling between electrons and phonons (polarons) is also responsible for the transport mechanism in insulating region which is modeled as:

$$\rho(T) = BT \exp\left(\frac{E_0}{k_B T}\right) \quad (2)$$

where B is a measure of ideal conductivity at elevated temperatures [23]. The polaron mediated hopping can also be fitted in the model [24]:

$$\rho(T) = \rho_0 T^{\alpha} \exp\left(\frac{E_0}{k_B T}\right) \quad (3)$$

where α is a constant whose valve is taken as 1.6 or 1.0 according to the nature of hopping process.

Some other reports suggest that the variable range hopping (VRH) model given by

$$\rho(T) = \rho_0 \exp\left(\frac{E_0}{k_B T}\right)^{1/4} \quad (4)$$

best describes the electronic transport in insulating region [25,26].

Fig. 6 shows variation of resistivity with Al^{3+} concentrations at different temperatures which makes it clear that at 325 K, the value of resistivity is highest for all concentrations. In the present study the $\ln(\rho)$ has been plotted against $10^3/T$. The plots for all samples show linear trend (Fig. 7) which can be best fitted in Eq. (1) and more or less acceptable by other described models. The activation energies calculated from the slopes of $\ln(\rho)$ vs $10^3/T$ plots range from 0.54 eV to 0.73 eV (Table 2) which suggest that the conduction in the insulating region is due to thermally assisted tunneling of charge careers through the grain boundary barrier and transition from donor level to conduction band [27].

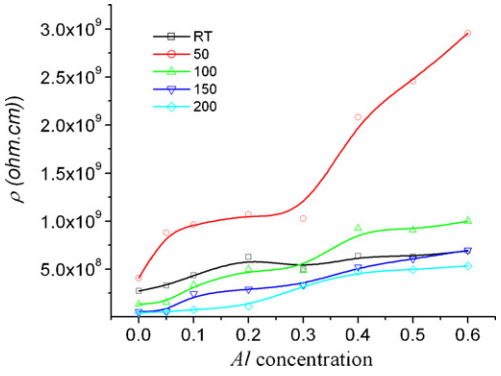

Fig. 6. Variation of resistivity with Al^{3+} concentration at different temperatures.

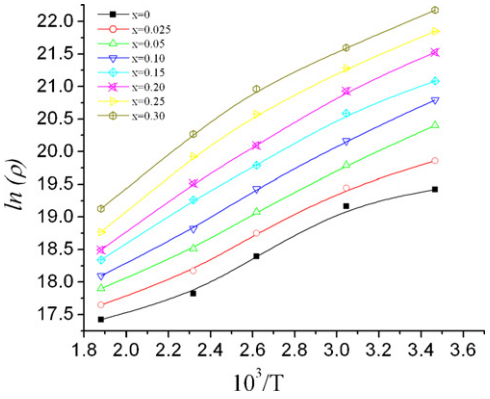

Fig. 7. Variation of $\ln(\rho)$ as a function of $10^3/T$.

Table 2
Variation of band gap and activation energy with composition.

x	Band gap (eV)	Activation energy (eV)
0.000	2.78	0.54
0.025	2.80	0.58
0.050	2.84	0.61
0.100	2.87	0.61
0.150	2.89	0.63
0.200	2.90	0.69
0.250	2.91	0.71
0.300	2.93	0.73

4. Conclusions

We have successfully synthesized Al^{3+} doped $BiFeO_3$ ceramics by combustion method. The X-ray patterns suggest that Al^{3+} ions have been successfully doped in the $BiFeO_3$ matrix and crystallite size varying from 13 nm to 19.6 nm. FTIR measurements confirm perovskite nature of the samples. All samples exhibit metal insulator transition temperature (T_{MI}) at 325 K. The resistivity is increasing with Al^{3+} concentration and follows the Arrhenius behavior. Activation energy was found to increase from 0.54 eV to 0.73 eV with doping. Optical band gap was observed to vary from 2.78 eV to 2.93 eV, which is higher compared to bulk BFO (1.82 eV). Higher values of band gaps for these ceramics are quite compatible with their high resistivities. The dielectric and impedance properties are subject to further study.

References

[1] S. Ghosh, S. Dasgupta, A. Sen, H.S. Maiti, J. Am. Ceram. Soc. 88 (2005) 1349–1352.
[2] J. Li, Y. Duan, H. He, D. Song, J. Alloys Compd. 315 (2001) 259–264.
[3] V.A. Khomchenko, D.A. Kiselev, E.K. Selenzeva, J.M. Vieira, A.M.L. Lopes, Y.G. Pogorelov, J.P. Araujo, A.L. Kholkin, Mater. Lett. 62 (2008) 1927–1929.

[4] Y. Lee, J. Wu, C. Lai, Appl. Phys. Lett. 88 (2006) 042903.
[5] C. Chen, J. Cheng, S. Yu, J. Cryst. Growth 291 (2006) 135–139.
[6] S.T. Zhang, M.H. Lu, D. Wu, Y.F. Chen, N.B. Ming, Appl. Phys. Lett. 87 (2005) 262907.
[7] C. Madhu, M.B. Bellakki, V. Manivannan, Indian J. Eng. Mater. Sci. 17 (2010) 131–139.
[8] B.D. Cullity, S. Stock, Elements of X-Ray Diffraction, 3rd ed., Prentice Hall, New Jersey, 2001, p. 303.
[9] J. Xu, G. Wang, H. Wang, D. Ding, Y. He, Mater. Lett. 63 (2009) 855–857.
[10] J.R. Chen, W.L. Wang, J.B. Li, G.H. Rao, J. Alloys Compd. 459 (2008) 66–70.
[11] V.A. Khomchenko, V.V. Shvartsman, P. Borisov, W. Kleemann, D.A. Kiselev, I.K. Bdikin, J.M. Vieira, A.L. Kholkin, J. Phys. D: Appl. Phys. 42 (2009) 045418.
[12] S. Farhadi, M. Zaidi, J. Mol. Catal. A: Chem. 299 (2009) 18–25.
[13] J. Lu, H. Yang, B. Liu, Mater. Res. Bull. 34 (1999) 2109–2116.
[14] V. Fruth, L. Mitoseriu, D. Berger, A. Ianculescu, C. Matei, S. Preda, M. Zaharescu, Prog. Solid State Chem. 35 (2007) 193–202.
[15] E.A.V. Ferri, I.A. Santos, E. Radovanovic, R. Bonzaninic, E.M. Girotto, J. Braz. Chem. Soc. 19 (2008) 1155.
[16] J. Xu, H. Kea, D. Jiaa, W. Wanga, Y. Zhoua, Philos. Mag. Lett. 9 (8) (2009) 704.
[17] S. Li, Y.H. Lin, B. Zhang, Y. Wang, C.W. Nan, J. Phys. C 114 (2010) 2906.
[18] C.M. Cho, J.H. Noh, I. Cho, J. An, K.S. Hong, J.Y. Kim, J. Am. Ceram. Soc. 91 (2008) 3753–3755.
[19] Z. Liu, Y. Qi, C. Lu, J. Mater. Sci.: Mater. Electron. 21 (2010) 380–384.
[20] J. Tauc, Amorphous and Liquid Semiconductors, Plenum Press, New York, 1974, p. 171.
[21] G.P. Joshi, N.S. Saxena, R. Mangal, A. Mishra, Bull. Mater. Sci. 26 (2003) 387–389.
[22] G.H. Jonker, J.H.V. Santen, Physica 19 (1953) 120–130.
[23] G. Jakob, W. Westerburg, F. Martin, H. Adrian, Phys. Rev. B 58 (1998) 14966.
[24] N.C. Yeh, R.P. Vasquez, D.A. Beam, C. Fu, J. Huynh, G. Beach, J. Phys.: Condens. Matter 9 (1997) 3713.
[25] N.F. Mott, Metal–Insulator Transitions, Taylor and Francis, London, 1974.
[26] J.M.D. Coey, M. Viret, L. Ranno, K. Ounadjela, Phys. Rev. Lett. 75 (1995) 3910.
[27] D. Patidar, K.S. Rathore, N.S. Saxena, K. Sharma, T.P. Sharma, Chalcogenide Lett. 5 (2008) 21–25.